Supplementary Materials for

Visible-frequency long-distance subwavelength focusing via surface plasmon hyperbolic polaritons (SPHPs)

Jianqiao Zhao[1]‡, Yuxin Zhang[2]‡, Xiaotian Xue[1]‡, Haodong Zhong[1], Tongzhou Xu[1], Yaolong Li[2], Jingbo Sun[3], Weipeng Wang[1], Ji Zhou[3], Shufeng Wang[2,4,5*], and Zhengjun Zhang[1*]*

[1] Key Laboratory of Advanced Materials (MOE), School of Materials Science and Engineering, Tsinghua University, Beijing 100084, China.

[2] State Key Laboratory for Mesoscopic Physics & Department of Physics, Collaborative Innovation Center of Quantum Matter & Frontiers Science Center for Nano-optoelectronics, Peking University, Beijing 100871, China.

[3] Key Laboratory of New Ceramics and Fine Processing, School of Materials Science and Engineering, Tsinghua University, Beijing 100084, China

[4] Peking University Yangtze Delta Institute of Optoelectronics, Nantong, Jiangsu 226010, China.

[5] Collaborative Innovation Center of Extreme Optics, Shanxi University, Taiyuan, Shanxi 030006, China.

‡ Authors contribute equally.

* Corresponding Authors: zjzhang@tsinghua.edu.cn; wangsf@pku.edu.cn; wpwang@tsinghua.edu.cn

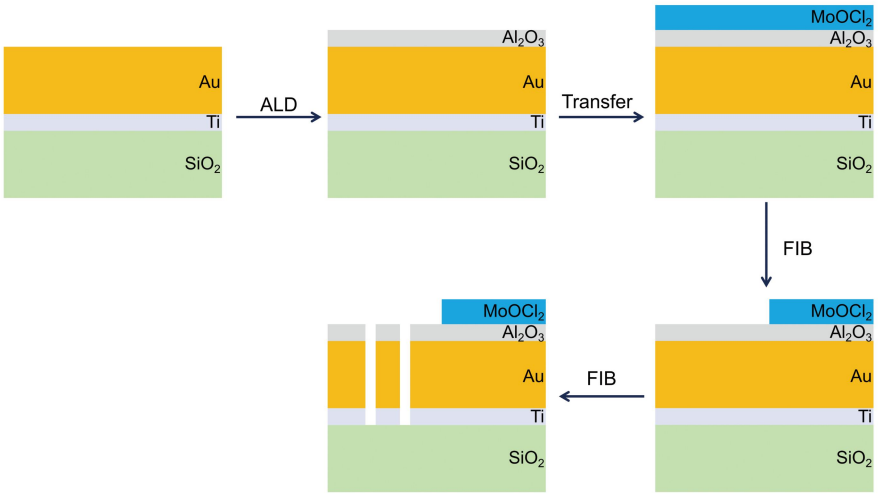

Figure S1. Sample fabrication process.

The fabrication process began with the sequential deposition of a 4 nm Ti adhesion layer and a 110 nm Au layer onto a quartz substrate using electron beam evaporation. Subsequently, a 2 nm Al_2O_3 layer was grown at 200°C via atomic layer deposition. The $MoOCl_2$ flakes with designated thicknesses were then transferred onto the substrate through a dry-transfer process.

To define the target nanostructure, a two-step focused ion beam (FIB) milling procedure was employed. In the first step, the $MoOCl_2$ layer was partially milled to expose the underlying Au film and to create a clean edge profile of the $MoOCl_2$, leaving a well-defined uncovered Au region for undisturbed surface plasmon polariton (SPP) propagation. In the second step, through-hole arrays were patterned into the exposed Au region to complete the nanostructure layout.

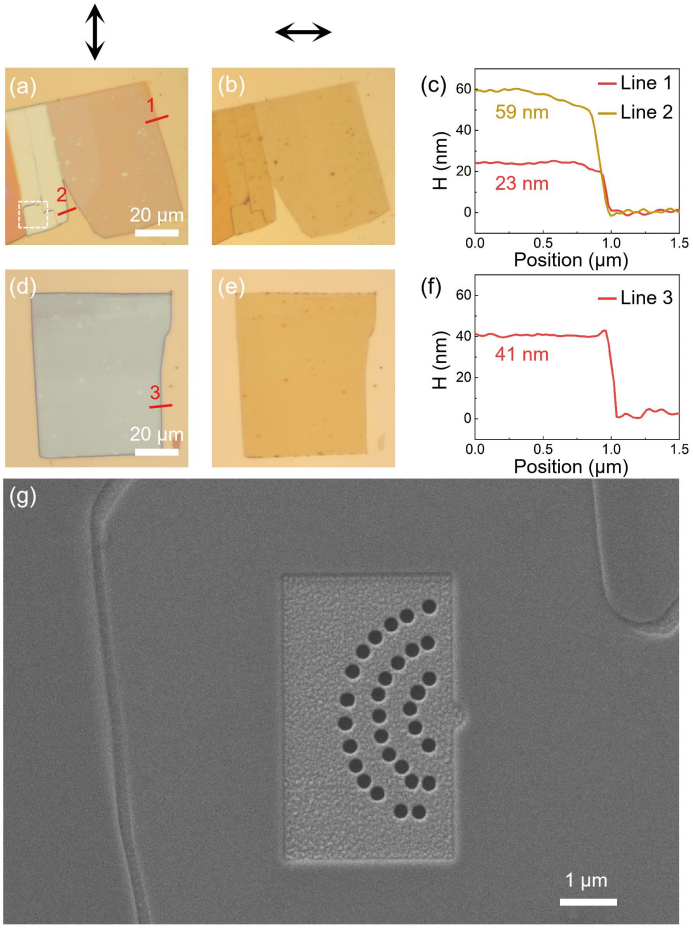

Figure S2. Sample characterization. (a,d) and (b,e) Optical images of transferred $MoOCl_2$ flakes on Au substrate under y- and x-polarized light (arrows indicate polarization direction). (c) and (f) Corresponding AFM height profiles. (g) Top-view SEM image of the FIB-patterned structure in the white dashed box in (a).

Optical images of $MoOCl_2$ flakes with different thicknesses transferred onto the Au substrate are shown in Figure S2(a,d) and (b,e) under y- and x-polarized illumination, respectively (polarization directions indicated by arrows at the top). Thicknesses of the three $MoOCl_2$ regions measured by atomic force microscopy (AFM) are shown in Figure S2(c) and (f), respectively. Figure S2(g) presents a top-view scanning electron microscope (SEM) image of the FIB-patterned structure fabricated within the white dashed box in Figure S2(a), showing the $MoOCl_2$ edge and the 30-hole metastructure on the exposed Au film.

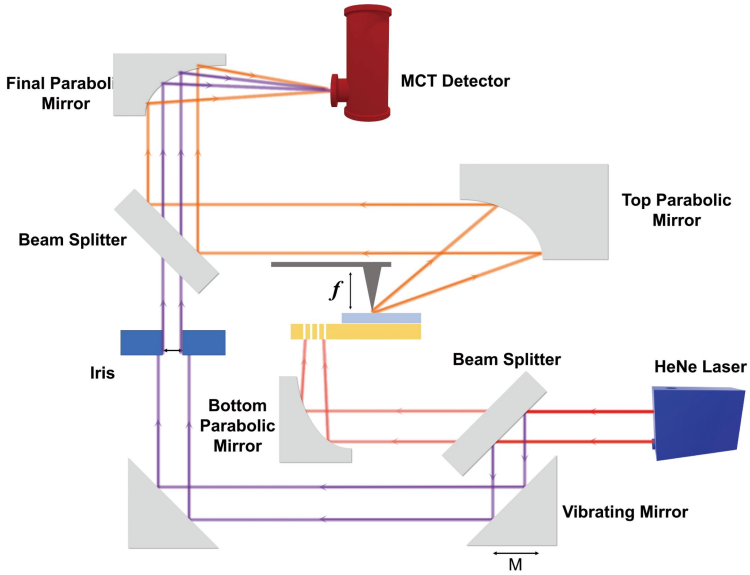

42

43 **Figure S3.** Complete transmission-mode SNOM setup for near-field measurements.

44 The transmission-mode SNOM setup for near-field measurements is shown in Figure S3, where
45 the laser beam is focused by a bottom parabolic mirror and vertically incident onto the bottom of
46 the sample, exciting the plasmonic responses of the Au nanostructure. The surface electric field is
47 scattered by the tip, collected by a top parabolic mirror, and ultimately directed towards a
48 photodetector for measurement. To improve sensitivity, pseudo-heterodyne demodulation is
49 implemented via an additional mirror vibration path, allowing extraction of higher-order near-field
50 signals. This configuration provides amplitude- and phase-resolved mapping of the near-field
51 distribution while effectively minimizing direct laser excitation and tip-induced field changes, thus
52 enabling clean SPP propagation and precise wavefront detection.

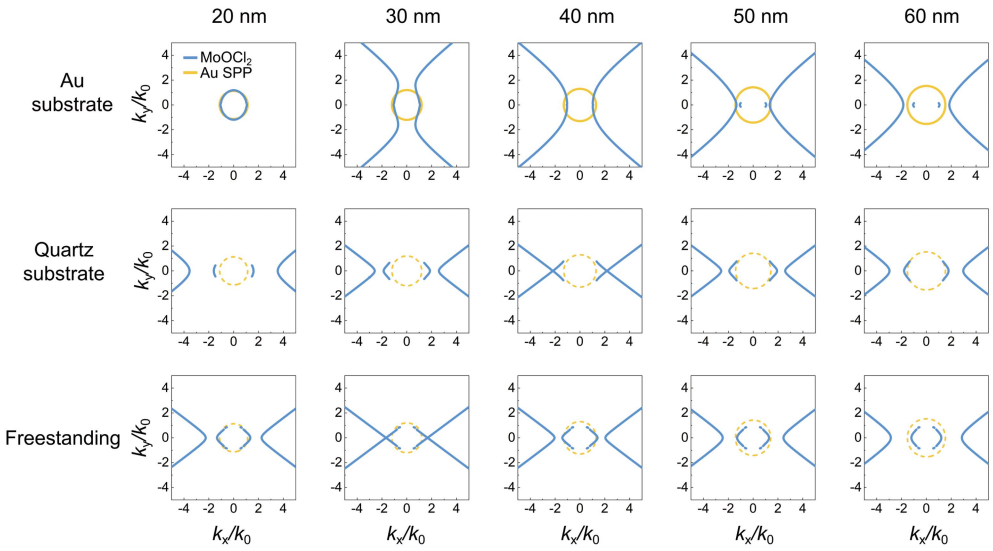

Figure S4. Thickness and dielectric environment dependent $MoOCl_2$ IFCs.

Figure S4 shows the calculated IFCs of $MoOCl_2$ on Au substrate, quartz substrate and in freestanding form for different thicknesses. Although the dielectric environment modifies the hyperbola shape, the hyperbolic vertices on quartz substrate and in freestanding case remain beyond k_{SPP}, indicating that intrinsic hyperbolic polariton modes are restricted to high-k components and cannot access lower wavevectors. In contrast, $MoOCl_2$ on the Au substrate supports hyperbolic modes at lower k within an appropriate thickness range, enabling effective wavefront control through the surface plasmon hyperbolic polariton (SPHP) mode.

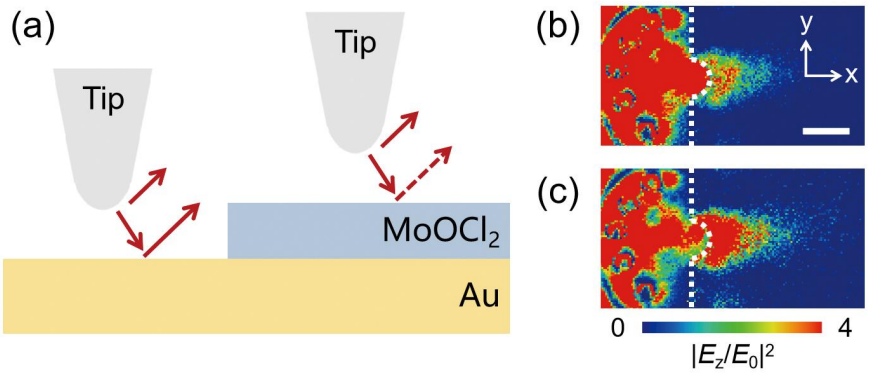

Figure S5. Quantitative correction for intrinsic near-field mapping. (a) Dielectric-induced signal contrast across different regions under transmission-mode SNOM detection. (b) Raw near-field electric field distribution measured by SNOM. (c) Intrinsic near-field electric field distribution after quantitative correction. Scale bar, 500 nm.

The detected SNOM signal contains a dielectric-dependent contribution arising from surface-reflected scattering, leading to artificial intensity contrast between Au and $MoOCl_2$ regions, as shown in Figure S5(a). By applying a quantitative correction method established in our previous work[1], this dielectric-induced disparity is removed, as shown in Figure S5(b) and (c), enabling reconstruction of the intrinsic near-field electric field distribution and allowing reliable comparison of absolute field intensities across different material regions.

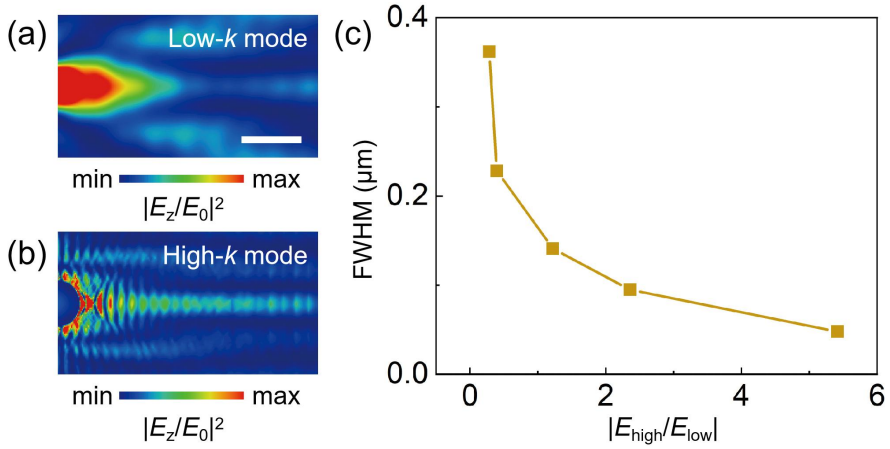

Figure S6. Momentum-resolved near-field analysis via FFT filtering. (a) and (b) Low-*k* and high-*k* near-field electric field distributions extracted by two-dimensional FFT filtering for the 40 nm $MoOCl_2$ sample, respectively. (c) FWHM of the focal spot as a function of the ratio $|E_{high}/E_{low}|$ for different $MoOCl_2$ thicknesses. Scale bar, 500 nm.

Two-dimensional fast Fourier transform (FFT) filtering of the simulation results is used to separate low- and high-momentum components of the surface electric field, as shown in Figure S6. The low-*k* component supports long-range propagation, while the high-*k* component provides strong spatial confinement. Their cooperative contribution enables long-distance subwavelength focusing. The monotonic decrease of the full width at half maximum (FWHM) with increasing $|E_{high}/E_{low}|$ demonstrates the critical role of high-*k* components in narrowing the focal spot.

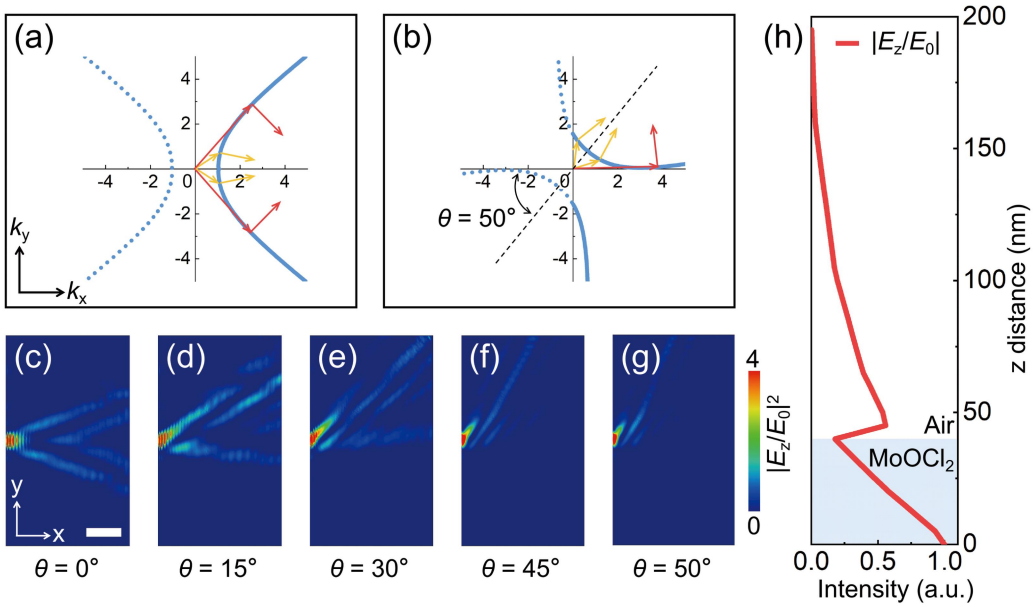

84

85 **Figure S7.** Separation of low-*k* and high-*k* components via crystal-axis rotation. (a) and (b) IFCs
86 at $\theta = 0°$ and 50°, with solid and dashed curves representing excitable and momentum-mismatched
87 modes, respectively. (c)-(g) Simulated field intensity distributions for $\theta = 0°$, 15°, 30°, 45°, 50°,
88 respectively. (h) z-profile of electric field at focus for the $\theta = 50°$ case. Scale bar, 1 μm.

89 Owing to the anisotropic hyperbolic dispersion, changing the angle θ between the crystal axis
90 and the incidence direction redirects the propagation of low-*k* and high-*k* modes, enabling
91 momentum-selective filtering. At $\theta = 0°$ (Figure S7(a)), both low-*k* and high-*k* modes are allowed
92 and jointly contribute to focusing, whereas at $\theta = 50°$ (Figure S7(b)) the high-*k* modes are steered
93 away from the $MoOCl_2$ region, leaving a pure low-*k* response. Corresponding simulated field
94 distributions in Figure S7(c)-(g) show a progressive suppression of high-*k* contributions with
95 increasing θ, which vanish above 45°. The z-profile of the focal field at $\theta = 50°$ (Figure S7(h))
96 confirms that the remaining signal is a hybrid surface mode dominated by metal-supported SPPs,
97 whose propagation is modulated by the in-plane hyperbolic dispersion of the $MoOCl_2$ layer.

Reference

1. Y. Fan et al., Direct measurement of the real strength of near-field electric field. *Appl. Phys. Lett.* **125**, 211105 (2024).